ELSEVIER

Materials Science and Engineering A 454–455 (2007) 433–440

MATERIALS SCIENCE & ENGINEERING A

www.elsevier.com/locate/msea

Modeling and experiments on the indentation deformation and recrystallization of a single-crystal nickel-base superalloy

C. Zambaldi [a], F. Roters [a], D. Raabe [a,*], U. Glatzel [b,1]

[a] *Max-Planck-Institut für Eisenforschung, Max-Planck-Strasse 1, 40237 Düsseldorf, Germany*

[b] *Metallische Werkstoffe, Universität Bayreuth, Ludwig-Thoma-Strasse 36b, 95440 Bayreuth, Germany*

Received 25 July 2006; received in revised form 8 November 2006; accepted 10 November 2006

Abstract

This study presents crystal-plasticity finite-element calculations of room temperature deformation of a single-crystal nickel-base superalloy and simulation results on the microstructural development during subsequent recrystallization. The predictions are compared to corresponding experiments. Single-crystalline material is deformed by Brinell-type indentation using a spherical indenter of 1 mm in diameter. A succeeding annealing under inert atmosphere leads to the formation of recrystallized grains around the indents. The crystal plasticity finite element method is used to predict the distribution of crystallographic slip around the indents. The amount of accumulated slip is used to estimate the stored deformation energy in the indented volume. A 2D probabilistic cellular automaton simulation is then applied to the predicted distribution of the stored energy for the simulation of the formation and growth of new grains around the indents. The cellular automaton predicts the kinetics, microstructures, and crystallographic texture evolving during recrystallization.

Keywords: Indentation topography; Primary recrystallization; CMSX-4; Electron backscattering diffraction (EBSD); Orientation mapping; Crystal plasticity Finite element method (CPFEM)

1. Introduction

Single-crystal components for aircraft gas-turbines have been established since the 1980s. Later they also found application in industrial gas-turbines. Single-crystal alloys were developed to overcome the limited mechanical performance of polycrystalline materials at high temperatures. Their superior creep resistance entailed an increased service temperature in the combustion chamber and thereby an improved overall efficiency of turbines. However, strain induced recrystallization is a long known problem in the production and service of nickel-base superalloy parts, since it is detrimental to their mechanical properties. If a sufficient plastic strain is imposed on single-crystal parts, such as turbine blades, during casting or machining, the solution heat treatment, which precedes the controlled precipitation of gamma prime particles, can lead to the formation of new grains. This effect is undesired since these grains may introduce disadvantageous orientations and high-angle grain boundaries. Besides such deformation-induced recrystallization phenomena occurring during manufacturing, any mechanical damage during service can lead to similar effects, which will reduce the life-time of the part and typically will act as nucleation site for fatigue cracks. Various previous publications have addressed such recrystallization mechanisms in single-crystal nickel-base alloys [1–8].

The strategies to characterize strain-induced primary recrystallization in such materials require, at first, a well-defined deformation step. Mostly indentation with different indenter geometries has been used for that (see Table 1). Such a deformation causes a high local dislocation density in the deformed regions of the single-crystal. During subsequent annealing the plastically deformed volume provides the driving force for nucleation and growth of new grains.

Obviously the inhomogeneous distribution of the stored energy of deformation is the key influence on the local grain nucleation and growth into the surrounding deformed material. Nevertheless, there is usually a lack of detailed knowledge about the amount and exact spatial distribution of the lattice defects introduced by the deformation step. This is the case especially

* Corresponding author. Tel.: +49 211 6792 278; fax: +49 211 6792 333.
E-mail address: d.raabe@mpie.de (D. Raabe).
[1] Tel.: +49 921 55 5555; fax: +49 921 55 5561.

0921-5093/$ – see front matter © 2006 Elsevier B.V. All rights reserved.
doi:10.1016/j.msea.2006.11.068

Table 1
Local deformation methods applied in earlier works on recrystallization of single-crystal nickel-base alloys

Alloys	Deformation methods	Reference
CMSX-2	Shot peening	[8]
CMSX-4	Spherical indentation, tension	[7]
CMSX-4, CMSX-2	Spherical indentation, die forging	[6]
CMSX-11B, PWA 1483, SRR 99, CMSX-6	Indentation (90°-prism), compression, low cycle fatigue	[5]
CMSX-6	Indentation (90°-prism, Vickers), low cycle fatigue	[4]
CMSX-6	Indentation (not specified)	[3]
CMSX-2, TMS12-2, TMS26	Grinding and sand blasting, tension	[2]
Ni9.5W8.5Cr5.5Al2.8Ta 2.2Ti0.015C (atom%)	Indentation (90°-prism), grit blasting	[1]

for indentation experiments, which lead to a highly non-uniform distribution of plastic strain. The present work aims at providing a more quantitative treatment of this problem by using first a crystal-plasticity finite-element simulation to predict the distribution of crystallographic slip around the indents, and secondly, a cellular automaton approach for the prediction of recrystallization in the vicinity of the indent.

2. Experimental investigation of primary recrystallization around spherical indents in single-crystal nickel-base superalloy CMSX-4

2.1. Experimental procedures

2.1.1. Single-crystal material

The second generation single-crystal alloy CMSX-4 in standard heat treated condition was used for the experiments. The composition is given in Table 2. The material exhibits a two-phase microstructure, i.e. it reveals coherent and cuboidal γ'-precipitates which are surrounded by γ-matrix. An approximate γ'-volume-fraction of 70% was determined by image analysis of a backscattered electron micrograph. The gamma prime phase has a $L1_2$ structure with the approximate chemical formula Ni_3Al. The gamma matrix phase is a solid solution with a face centered cubic (fcc) structure. The size of the cuboidal precipitates is in the range of 0.5 μm. The material has a dendritic cast microstructure with a primary dendrite spacing of about 250 μm.

Table 2
Nominal composition of alloy CMSX-4 as given in [9]

Element	wt.%
Ni	Balance
Co	9
Cr	6.5
Ta	6.5
W	6
Al	5.6
Re	3
Ti	1.0
Mo	0.6
Hf	0.1

2.1.2. Deformation by spherical indentation

Six samples with dimensions of 15 mm × 20 mm × 8 mm were cut by spark erosion. The 15 mm × 20 mm faces were aligned parallel to the (0 0 1) crystallographic planes within 8° maximum deviation. On each sample 20 indents were made with a cemented carbide ball of 1.0 ± 0.003 mm in diameter. The indents were grouped in four rows, each containing five indents with identical loads. The indentation loads were 0.49 kN, 0.98 kN, 1.47 kN, and 1.84 kN, respectively. The minimum distance between the axes of the indents was 3 mm.

2.1.3. Optical surface topography of the indents

The height profile of the indented surface was measured using a non-contact optical measurement device. The laser profilometry unit employed a 780 nm laser source and the vertical resolution of the device was 0.1 μm. This approach allowed for a quantified representation of the anisotropic pile-up patterns evolving during indentation with different loads.

2.1.4. Recrystallization annealing treatment close to the gamma prime solvus temperature

The samples were annealed at temperatures 1240 °C, 1260 °C and 1280 °C. The annealing times were 30 min and 120 min, respectively, which gives a set of six different annealing procedures. In order to avoid oxidation, the samples were tubed in silica glass under inert argon atmosphere. The furnace has been preheated and cooling was done in air. In the chosen temperature range a strong decrease in γ'-volume-fraction was to be expected from thermodynamic calculations [7] and differential thermal analysis [6]. For comparison, a similar temperature dependence of the gamma-prime volume-fraction of another superalloy (SRR 99) has been determined experimentally by Schmidt and Feller-Kniepmeier [10].

2.1.5. Metallographic preparation and evaluation

After the recrystallization annealing treatment the indented surfaces of the samples were polished. The recrystallization kinetics were evaluated with respect to the recrystallized area around the indents in the plane of the formerly undeformed surface. Care was taken to achieve a constant remaining diameter of the indents for each indentation load. By etching in Kalling's reagent (2 g $CuCl_2$, 40 ml HCl, 40 ml ethyl alcohol, 40 ml H_2O) for three to five seconds the structure of the newly formed grains became visible. The recrystallized region was photographed in a light microscope and the cross-sectional recrystallized area was measured using standard image analysis software. For each of the six annealing procedures five indents were evaluated for each indentation load.

2.1.6. Orientation mapping in the scanning electron microscope

Several indents were analyzed by orientation microscopy by means of an electron backscatter diffraction system (EBSD) in a field-emission-gun scanning electron microscope (FEG-SEM).

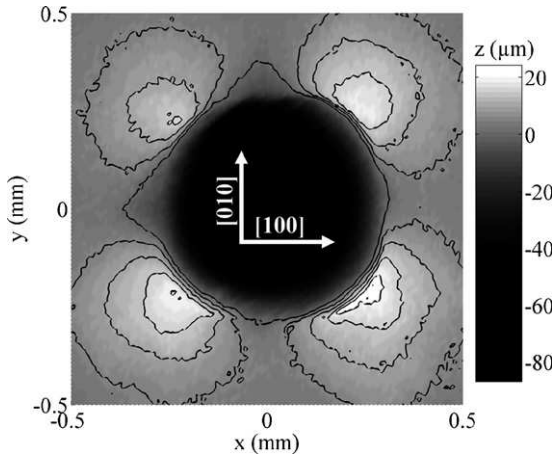

Fig. 1. Surface topography of an 1.47 kN-indent determined by laser profilometry. Indentation depth is 88 μm. The [1 0 0] and [0 1 0] crystal axes are aligned to the *x*- and *y*-axis. The contour lines show heights in 5 μm steps starting from the 0 μm level of the formerly undeformed surface.

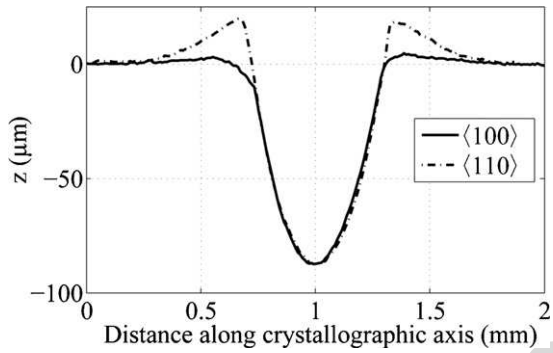

Fig. 2. Cross-sectional height profile of an indent in [1 0 0] and [1 1 0] directions. Indentation load is 1.47 kN, indentation depth is 88 μm. The height to width axes ratio is 10:1.

The step size was 6 μm. High-angle and low-angle grain boundaries, as well as annealing twins could be identified. Details of the microstructure were analyzed with a higher resolution to investigate the γ/γ′-coherency in the recrystallized area.

2.2. Experimental results and discussion

Fig. 1 shows the height profile created by a 1.47 kN-indent. Apparent is the strong pile-up anisotropy. It reflects the four-fold crystallographic symmetry around the [0 0 1] indentation axis. While in [1 0 0]-directions[1] almost no bulging out of the material is observed, strong pile-ups are formed along the [1 1 0]-directions (see Fig. 2). This is in agreement with the pile-up behavior of superalloys and fcc metals reported in earlier studies [11–13].

Fig. 3 shows the time and temperature dependence of the recrystallized area around an 1.47 kN indent. A strong temperature dependence of the recrystallized area exists in the applied

[1] The notation [*uvw*] indicates that only permutations of *u* and *v* are allowed, while *w* is fixed.

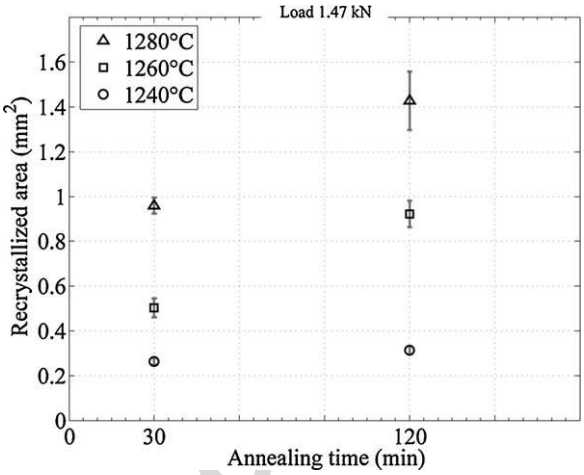

Fig. 3. Time and temperature dependence of the recrystallized area around an 1.47 kN indent in a (0 0 1) cross-section corresponding to the formerly undeformed surface. Also shown is the standard deviation calculated from the five measured values.

range. This can be explained by the inhibiting effect of the γ'-precipitates on the movement of grain boundaries. The precipitate volume-fraction decreases rapidly from about 50% at 1100 °C to zero at just above 1300 °C (see calculations in [7]). Therefore, the mobility of the high-angle grain boundaries will increase drastically in this temperature range.

At 1280 °C larger scatter for the measured areas is observed for the 2 h annealing as expressed by the higher standard deviation in Fig. 3. This holds also for the other three indentation loads (not shown here). The scatter observed for the recrystallized area can be understood in terms of the smaller number of grains, i.e. successful nuclei, at higher temperatures (see Fig. 11). The orientations of the nuclei lead to high-angle grain boundaries of different mobilities. While in the case of many recrystallized grains, i.e. at temperature 1240 °C, the variety of grain-boundary mobilities will level out in the global value of recrystallized area, for a relatively small number of successful nuclei their difference in growth rate does not level out, but instead can still be observed in the overall kinetics of the respective arrangement of nuclei.

Fig. 11 shows some typical orientation microscopy results measured after recrystallization. After annealing at 1240 °C the lattice rotation introduced by the indentation is still visible outside a thin shell of fine-grained recrystallized material.

At 1240 °C and 30 min some information about the nucleation behavior can be gained: Small grain sizes are observed in the [1 1 0]-directions, where also the highest pile-up and highest intensity of slip-lines would occur after indentation. This implies a higher nucleation rate in these areas. In the [1 0 0]-directions larger grains are formed because of a lower nucleation rate. However, the overall amount of recrystallized material is higher in the region where the number of nuclei was higher, i.e. where the grains were smaller.

For the annealing procedures used in the experiments no incoherency between γ and γ′ was found in the recrystallized grains, as reported for the cellular recrystallization at lower temperatures [4,5].

3. Crystal-plasticity finite-element model to estimate the stored energy around a spherical indent in a single-crystal nickel-base superalloy

3.1. Deformation behavior of the single-crystal nickel-base superalloy

The deformation behavior of single-crystal nickel-base superalloys strongly depends on the temperature. The acting mechanisms and their temperature dependence are discussed for example in [7,14]. In the present work the coherent fcc/$L1_2$ microstructure is treated as homogeneous, face centered cubic material with slip occurring on the 12 $\{1\,1\,1\}\langle 1\bar{1}0\rangle$ slip systems. As Cox et al. pointed out [7], at room temperature, the flow stress of Ni_3Al is only about one fifth of the flow stress of the superalloy. Therefore the precipitates are expected to deform with the matrix.

It has been shown [14] that additional slip systems are operating during high-temperature deformation. Therefore, the treatment at hand is limited to room temperature.

3.2. Spherical indentation of single-crystals

The general case of spherical indentation in fcc metals has been mostly studied on copper [12,15–19]. Okazaki et al. [6] conducted an analysis of the resolved shear stresses on the octahedral slip systems around the indent. Their calculations were based on the assumption that the stress state around the indenter could be described by the analytical solution for a sphere cavity expanding in an infinite isotropic solid.

3.3. Kinematics and constitutive equations

The crystal-plasticity finite-element method (CP-FEM) has been shown to be capable of describing metal forming problems in a detailed way, e.g. [20,21]. The underlying kinematic and constitutive equations are defined in the works of Kalidindi et al. [22,23] and the references therein, e.g. [24–26], as well as in other classical papers in that field [27,28]. Additionally to the mathematical and numerical treatment of the deformation behavior following [22], an anisotropic constitutive law instead of an isotropic one was employed for the elastic stresses.

Multiplicative decomposition of the deformation gradient, $\mathbf{F}$, into its plastic and elastic part is used for the treatment of finite deformations:

$$\mathbf{F} = \mathbf{F}^{\mathrm{e}}\ \mathbf{F}^{\mathrm{p}}. \tag{1}$$

The flow rule for the plastic deformation gradient, $\mathbf{F}^{\mathrm{p}}$, is given by

$$\dot{\mathbf{F}}^{\mathrm{p}} = \mathbf{L}^{\mathrm{p}}\ \mathbf{F}^{\mathrm{p}}, \tag{2}$$

with $\mathbf{L}^{\mathrm{p}}$ denominating the plastic velocity gradient. It is assumed to consist of the sum of the shear rates, $\dot{\gamma}^{\alpha}$, over the number of considered slip systems, with $\mathbf{S}_0^{\alpha}$ being the Schmid–Matrices. The superscript α specifies the slip system:

$$L^{\mathrm{p}} = \sum_{\alpha} \dot{\gamma}^{\alpha} \mathbf{S}_0^{\alpha} \tag{3}$$

$\mathbf{S}_0^{\alpha}$ is constructed by $\mathbf{S}_0^{\alpha} = \mathbf{m}_0^{\alpha} \otimes \mathbf{n}_0^{\alpha}$, where $\mathbf{m}_0^{\alpha}$ denotes the slip direction of slip system α and $\mathbf{n}_0^{\alpha}$ the respective slip plane normal. The shear rates $\dot{\gamma}^{\alpha}$ are taken to evolve as

$$\dot{\gamma}^{\alpha} = \dot{\gamma}_0 \left| \frac{\tau^{\alpha}}{s^{\alpha}} \right|^{1/m} \mathrm{sign}(\tau^{\alpha}), \tag{4}$$

with the material parameters reference shearing rate, $\dot{\gamma}_0$, and shear rate sensitivity, m. The resolved shear stresses are denominated by τ^{α}, and s^{α} are the slip resistances. The slip resistances are given the same initial value, s_0, for all slip systems and their evolution is calculated from:

$$\dot{s}^{\alpha} = \sum_{\beta} q^{\alpha\beta} h^{(\beta)} |\dot{\gamma}^{\beta}|, \tag{5}$$

where the intensity of latent- and self-hardening of the slip systems is governed by the single slip hardening rates, $h^{(\beta)}$, and the ratio $q^{\alpha\beta}$, which is assumed to be 1.0 for coplanar and 1.4 for non-coplanar slip systems [26]. The evolution of the single slip hardening rates is, in a saturation form, given by

$$h^{(\beta)} = h_0 \left\{ 1 - \frac{s^{\beta}}{s_{\mathrm{s}}} \right\}^{a}, \tag{6}$$

with hardening parameters h_0, s_{s} and hardening exponent a.

3.4. Compression tests for model calibration

Room temperature uniaxial compression tests have been performed on [0 0 1]-oriented cylindrical samples. Sample height and diameter were both 4 mm. Ceramic dies were used because of the superalloy's high hardness and strong work hardening. The compression flow-curves were used to calibrate the crystal-plasticity model. The flow-curves of the compression tests and their computational analogue are shown in Fig. 4.

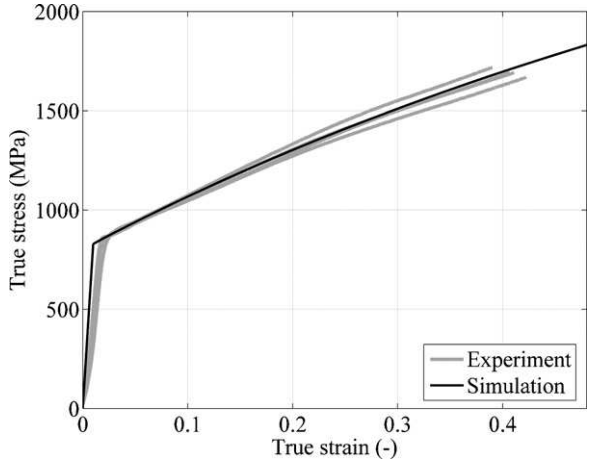

Fig. 4. Room temperature compression test of [0 0 1] oriented cylindrical samples. The bold gray lines show four experimental curves and the black line the result of a computational analogue of the compression test with fitted parameters.

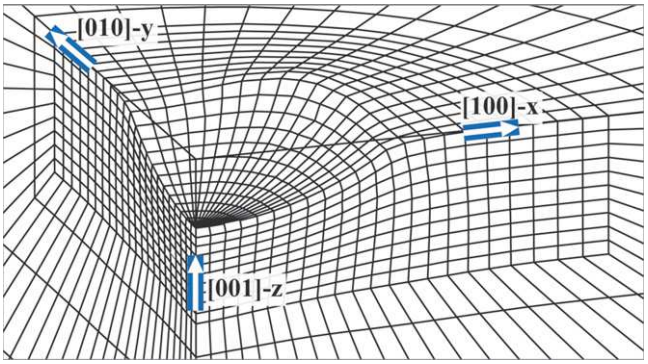

Fig. 5. The deformed finite element mesh in the region of interest. The simulated indentation depth is 0.1 mm. Pronounced pile-up is found in the [1 1 0] direction.

3.5. Finite-element modeling strategy for the single-crystal (0 0 1) spherical indentation problem

In this basic analysis the single orientation [0 0 1] was chosen as indentation axis. Therefore a quarter-cylindrical model was sufficient[2] due to the four-fold crystallographic symmetry (Fig. 5). A hexahedral mesh was generated axially symmetric around the indentation axis. This ensured that all anisotropy observed in the simulation results would originate from the constitutive law. The radius of the modeled volume amounted to 2.5 mm, its height in indentation z-direction was 1.6 mm.

The indenter was modeled as a rigid half-sphere. The range of considered indentation depths did not exceed a tenth of the indenter diameter D of 1.0 mm. For the simulation the influence of friction was assumed to be negligible. However, it should be mentioned that a dependency of the pile-up patterns from Coulomb friction coefficients in the range of 0–0.4 has been reported for calculations on mono-crystalline copper [16].

The indenter motion was displacement-controlled through defining a velocity profile which resulted in a smooth time–displacement curve. The average indenter velocity in all simulations amounted to 0.01 mm/s.

3.6. CP-FEM results and discussion

The material model parameters used for the simulations are given in Table 3. The identified set of parameters was used to calculate a three-dimensional crystal-plasticity finite-element (CP-FE) model of spherical indentation.

Different comparisons between the experimental results and the simulations can be drawn. One important and readily observable characteristic of the indents is the deformation of the free surface, which has already been discussed in the experimental section above. Fig. 6 shows the comparison between the experimental and simulated pile-up in the [1 0 0] and [1 1 0] crystallographic directions. Good agreement is observed at indentation depths larger than 80 μm.

[2] In principle it is possible to reduce the modeled volume to an eighth. The decision to not fully exploit the cubic symmetry was based on the resulting possibility to readily verify the symmetric response of equivalent slip systems.

Table 3
Material model parameters for single-crystal CMSX-4, derived from the [0 0 1] uniaxial compression tests; elastic constants were taken from [29]

Parameter	Symbol	Value	Unit
Elastic constant	C_{11}	252	GPa
Elastic constant	C_{12}	161	GPa
Elastic constant	C_{44}	131	GPa
Strain rate sensitivity	m	0.05	n/a
Reference shearing rate	γ_0	0.001	1/s
Initial slip resistance	s_0	350	MPa
Saturation slip resistance	s_s	1500	MPa
Hardening parameter	h_0	550	MPa
Hardening exponent	a	1.3	n/a
Coplanar hardening ratio	$q^{\alpha\beta}$	1.0	n/a
Non-coplanar hardening ratio	$q^{\alpha\beta}$	1.4	n/a

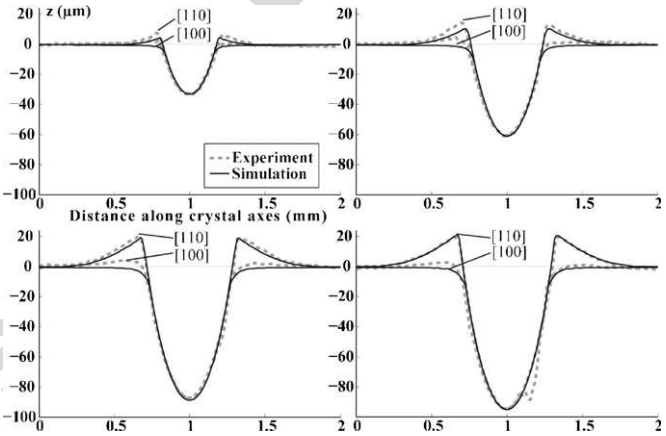

Fig. 6. Comparison of experimental and simulated topography of the indents. Each diagram depicts height profiles in the two directions [1 1 0] and [1 0 0]. Generally a pronounced pile-up is observed in the [1 1 0] direction. The height to width axes aspect ratio is 10:1.

The simulated load-displacement curve of the indenter is shown in Fig. 7 together with the experimental data points. At 0.49 kN 83% of the experimentally applied force is predicted. This fraction drops to 73% at a load of 1.84 kN. The growing discrepancy between the experimental and the simulated force could be due to several reasons. At first, a calibration of

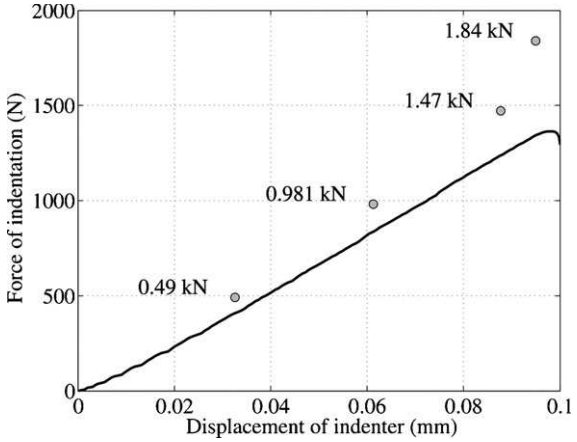

Fig. 7. Force displacement curve of the simulated indentation. The experimental values are shown as filled circles.

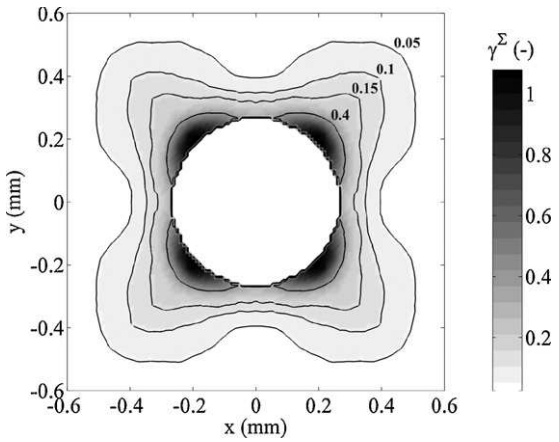

Fig. 8. Simulated profile of accumulated slip around an 1.47 kN indent, 10 μm below the initially undeformed sample surface plane. Contour lines are drawn at slip levels 0.05, 0.1, 0.15 and 0.4. The mark of the indenter has a diameter of 530 μm.

the constitutive parameters for more than one orientation would possibly have improved the constitutive description, because for the complex deformation by indentation dislocation glide is activated in a highly localized and non-linear fashion. Second, the discrepancy could be explained by the fact that the model does not incorporate strain-gradient hardening contributions. When deforming a metal by indentation, usually large local lattice curvatures in the vicinity of the indent will occur in the plastic zone. Therefore an additional hardening contribution arises from geometrically necessary dislocations (GNDs) preserving lattice continuity [30]. In the authors' opinion friction effects will not significantly influence the load-displacement response during indentation to depths considered here.

Another result of the CP-FE analysis is the amount of accumulated slip in the indented material. It was used to prepare input data for the cellular automaton predictions of the microstructural evolution during heat treatment which are presented in the ensuing section. The accumulated slip is calculated from summing up the amount of shear over all slip systems. In accordance with the pile-up behavior, this scalar value is distributed in a highly anisotropic fashion around the indent (see Fig. 8). Its maximum values correspond to the locations of the most pronounced formation of slip-lines on the sample surface, which are also the directions of maximum pile-up.

4. Cellular automaton simulation of primary static recrystallization in an indented single-crystal: kinetics and microstructure

4.1. Two-dimensional cellular automaton model

The profile of the accumulated plastic slip, shown in Fig. 8, was used as input data set for the recrystallization simulation by the cellular automaton method. For this purpose, the square cross-section was subdivided into an array of 200 × 200 cells and each of them was assigned a scalar value of the stored energy of deformation. The local values of the stored deformation energy were expressed in terms of a reference dislocation density of 10^{15} m^{-2} which was multiplied by the local amount of accumulated shear. Nucleation of new grains was dealt with on a statistical basis (see section below). In nucleating cells the dislocation density was dropped to zero and a random orientation was assigned to them.

In each time step of the cellular automaton, all neighbors of already recrystallized cells had a certain probability to also recrystallize and thereby inherit the orientation of the adjacent recrystallized cell. This probability was dependent on the crystallographic misorientation between the two cells and on the difference in stored energy. Only high-angle grain boundaries with a misorientation above 15° were assumed to move, i.e. to switch neighboring cells. The mobility of a high-angle grain boundary was taken not to be dependent from other characteristics of the boundary, such as coincident site lattice configurations.

In the CP-FEM result, the iso-surfaces of accumulated slip were approximately perpendicular to the cross-section that provided the input data for the cellular automaton. This means that the cross-section profile of the accumulated slip did not vary along the indentation direction in the volume close to the sample surface. Therefore in the cross-section under consideration a two-dimensional simulation of the microstructural evolution was sufficient.

Details of the probabilistic cellular automaton technique and its combination with crystal plasticity finite element simulations can be found in earlier works [31,32].

4.2. Model of continuous nucleation

A description of the possibly operating nucleation by subgrain coalescence can be found in [33]. However, the exact steps of nucleation are unclear in the studied alloy. Therefore, a phenomenological model was implemented and fitted to describe the experimentally observed nucleation behavior. The nucleation rate was assumed to depend essentially on the amount of accumulated slip, γ^{Σ}. High local values of the accumulated slip correspond to a high dislocation density and hence to an increased driving force for the formation of viable nuclei.

The statistical nucleation model was formulated using a Weibull probability distribution function, Eq. (7), which results in low nucleation probabilities for regions with minor shear and high nucleation rates for highly sheared material.

$$w_{\mathrm{nuc}} = C_{\mathrm{nuc}}\ \Delta t \left(1 - \exp\left[-\left(\frac{\gamma^{\Sigma}}{b}\right)^{c}\right]\right) \tag{7}$$

The above relation is depicted in Fig. 9, where w_{nuc} is the scaled nucleation probability for one cell. C_{nuc} is a scaling factor, which allows to directly control the overall number of formed nuclei and was used to fit the nucleation rate in the simulations. C_{nuc} was 6×10^{-4} for all simulations presented in the following. Δt is the time step of the automaton and ensures a constant nucleation behavior for different time steps. The parameters b and c control the shape of the curve. Chosen to reproduce the experimental kinetics (Fig. 10) and microstructures (Fig. 11), b and c were taken to be 0.68 and 6.0, respectively. At each time step of the

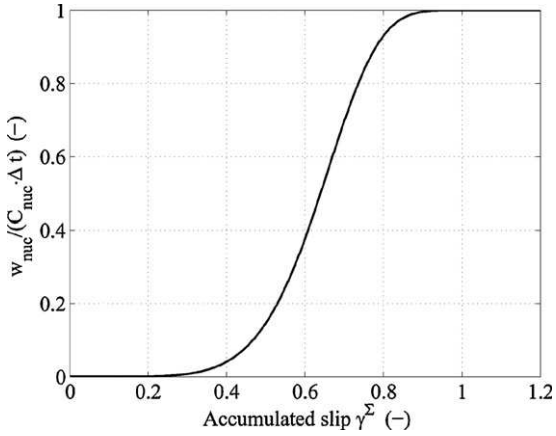

Fig. 9. Normalized nucleation probability $w_{\mathrm{nuc}}/(C_{\mathrm{nuc}}\ \Delta t)$ against accumulated slip; the shape parameters are $b = 0.68$ and $c = 6$.

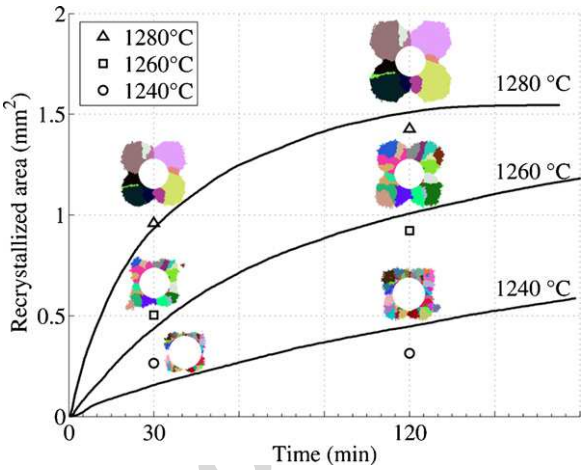

Fig. 10. Kinetics of the simulation in comparison to the experimental values. The recrystallized area is measured, respectively, simulated just below the formerly undeformed (0 0 1) surface of the single-crystal material. Also shown are the corresponding simulated microstructures with random grain coloring and arbitrary scaling (the indent cross-section is 530 μm diameter).

cellular automaton, the nucleation condition is tested in a Monte-Carlo step for each non-recrystallized cell. If the probabilistic condition:

$$\mathrm{rand}(\ ) < w_{\mathrm{nuc}} \tag{8}$$

is fulfilled, a random orientation is assigned to the cell and its stored energy is set to zero.

Although nuclei could in principle form during the whole duration of the simulated annealing procedure, nucleation was actually relevant only in the beginning of the recrystallization simulations. The highly sheared regions, where most of the nucleation took place, had been consumed

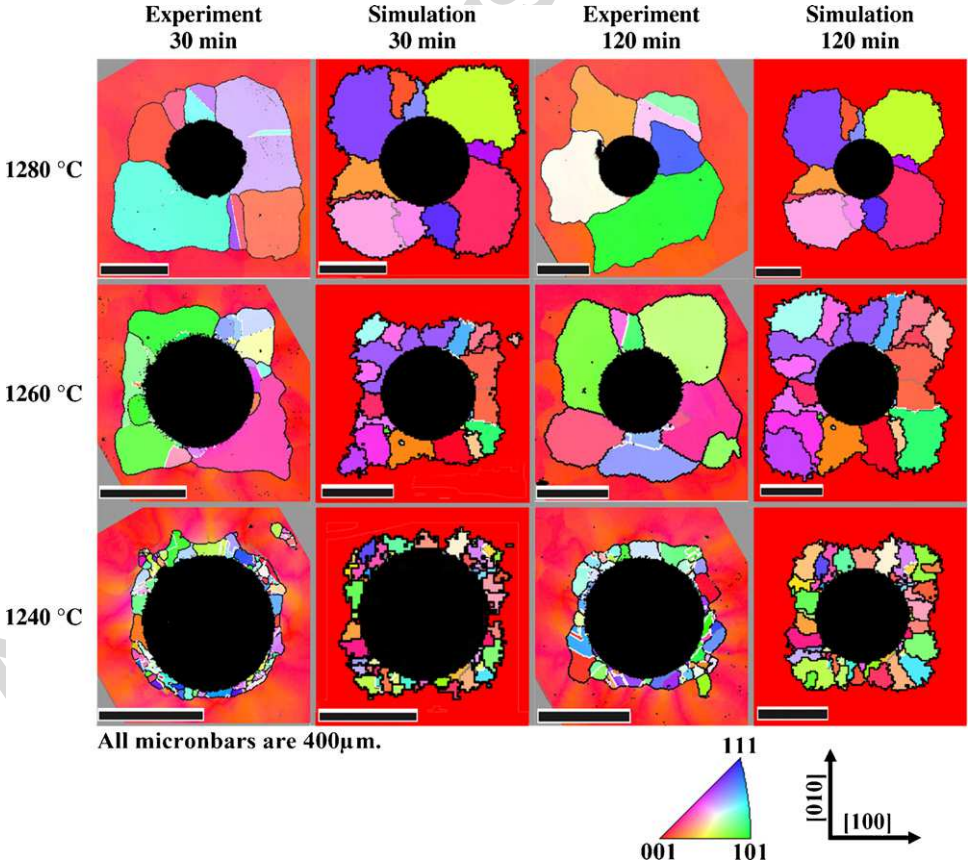

Fig. 11. Simulation results, showing possibly evolving microstructures, compared to EBSD measurements. The orientations are colored in terms of a 0 0 1 inverse pole figure coloring scheme as shown in the legend. The arrows indicate the orientation of the parent material. White lines in the experimental results indicate Σ3 annealing twins, black lines are used for high angle grain boundaries with a misorientation of more than 15°.

to a large extend by grain growth after a few simulation steps.

4.3. Kinetics and grain structure of the simulation results

In the temperature range from 1240 °C to 1280 °C, a very large rise in the mobility of the high angle grain boundaries was observed experimentally. The temperature dependency of the mobility was incorporated into the cellular automaton with the Arrhenius formula $M = M_0 \exp[-Q/RT]$. For all simulations presented here, the pre-exponential factor M_0 was set to 10^{31} m^3/Ns and the activation energy Q was taken to be 1290 kJ/mol. The resulting simulated growth kinetics, in terms of recrystallized area, is illustrated in Fig. 10 which also shows the experimentally measured kinetics.

It should be noticed that the activation energy, necessary to fit the experimental data, was at least one order of magnitude higher compared to the values applicable to single-phase pure metals (see e.g. [34]). This reflects the major role of the dissolving γ'-phase in the migration of high-angle grain boundaries in this class of alloys. The high activation energy should, therefore, be considered as a phenomenological parameter, which includes not only the thermal activation of the atomic movements, but also the phase dissolution effect. In addition, it should be mentioned that Porter and Ralph [35] reported a high activation energy of 790 kJ/mol for recrystallization experiments on a warm-rolled polycrystalline Nimonic 115 alloy.

The agreement between the simulated and the experimentally observed microstructures, shown in Fig. 11, is good despite the fact that in the simulation the influence of static recovery and the dependence of the grain boundary mobility on the boundary plane inclination and misorientation were neglected. The dependence of the grain boundary mobility on the misorientation angle was not incorporated in the simulations simply due to a lack of experimental data. Recovery mechanisms were not included, because earlier experiments have shown that this effect is very weak in these materials [5]. Furthermore, the formation of annealing twins was not taken into account in the model, though it might play an important role for the generation of the observed quasi-random orientations, e.g. [36–38].

5. Conclusions

An integrated simulation strategy for the characterization of primary recrystallization was developed and applied to a second generation single-crystal nickel-base superalloy. By using a crystal plasticity finite element approach, the driving force for nucleation and grain growth around a Brinell-type indent was modeled. The crystal-plasticity approach was validated by comparison to the experimentally observed pile-up behavior and the load-displacement curve obtained from the indentation test. The crystal plasticity material parameters were fitted to uniaxial compression data of a corresponding single-crystal. Good agreement between experiment and simulation was obtained for the anisotropic pile-up pattern.

A subsequent annealing process, leading to the formation of new grains via primary recrystallization, was simulated by using a probabilistic cellular automaton that employed a continuous nucleation model. This simulation was not only reflecting the kinetics of primary recrystallization, but it was also capable to match the experimentally observed recrystallization microstructures.

References

[1] S.D. Bond, J.W. Martin, J. Mater. Sci. 19 (1984) 3867–3872.
[2] Y. Ohta, Y.G. Nakagawa, J. Tsuji, J. Jpn. Inst. Met. 54 (1) (1990) 84–92.
[3] U. Paul, P.R. Sahm, Mater. Sci. Eng. A 173 (1993) 49–54.
[4] P.D. Portella, W. Österle, in: H. Mughrabi, G. Gottstein, H. Mecking, H. Riedel, J. Tobolski (Eds.), Microstructure and Mechanical Properties of Metallic High-Temperature Materials, DFG Research Report, 1999, pp. 441–453 (Chapter 31).
[5] R. Bürgel, P.D. Portella, J. Preuhs, in: T.M. Pollock, R.D. Kissinger, R.R. Bowman, K.A. Green, M. McLean, S.L. Olson, J.J. Schirra (Eds.), Superalloys 2000, TMS, Warrendale, 2000, pp. 229–238.
[6] M. Okazaki, A.T. Hiura, T. Suzuki, in: T.M. Pollock, R.D. Kissinger, R.R. Bowman, K.A. Green, M. McLean, S.L. Olson, J.J. Schirra (Eds.), Superalloys 2000, TMS, Warrendale, 2000, pp. 505–514.
[7] D.C. Cox, B. Roebuck, C.M.F. Rae, R.C. Reed, Mater. Sci. Technol. 19 (2003) 440–446.
[8] C.-Y. Jo, H.-Y. Cho, H.-M. Kim, Mater. Sci. Technol. 19 (2003) 1665–1670.
[9] Cannon-Muskegon Corporation, url: http://www.c-mgroup.com/vacuum_melt_index/nickel_base_sx.htm, March 2005.
[10] R. Schmidt, M. Feller-Kniepmeier, Scripta Metall. Mater. 26 (12) (1992) 1919–1924.
[11] P. Peralta, R. Ledoux, R. Dickerson, M. Hakik, P. Dickerson, Metall. Mater. Trans. A 35 (2004) 2247–2255.
[12] Y. Wang, D. Raabe, C. Klüber, F. Roters, Acta Mater. 52 (2004) 2229–2238.
[13] B. Eidel, F. Gruttmann, Proc. Appl. Math. Mech. 5 (2005) 265–266.
[14] M. Feller-Kniepmeier, T. Link, I. Poschmann, G. Scheunemann-Frerker, C. Schulze, Acta Mater. 44 (1996) 2397–2407.
[15] L.D. Dyer, Trans. ASM 58 (1965) 620–644.
[16] Y. Liu, B. Wang, M. Yoshino, S. Roy, H. Lu, R. Komanduri, J. Mech. Phys. Solids 53 (2005) 2718–2741.
[17] A.L. Coulet, F. Minari, L. Capella, Scripta Metall. 4 (1970) 593–598.
[18] F. Minari, Y. Maurissen, B. Pichaud, P. Bellandi, Scripta Metall. 4 (1970) 843–848.
[19] N. Zaafarani, D. Raabe, R.N. Singh, F. Roters, S. Zaefferer, Acta Mater. 54 (7) (2006) 1863–1876.
[20] A.J. Beaudoin, P.R. Dawson, K.K. Mathur, U.F. Kocks, D.A. Korzekwa, Comput. Methods Appl. Mech. Eng. 117 (1994) 49–70.
[21] F. Roters, Comp. Mater. Sci. 32 (3–4) (2005) 509–517.
[22] S.R. Kalidindi, C.A. Bronkhorst, L. Anand, Int. J. Mech. Sci. 34 (4) (1992) 309–329.
[23] S.R. Kalidindi, C.A. Bronkhorst, L. Anand, J. Mech. Phys. Solids 40 (1992) 537–569.
[24] D. Pierce, R.J. Asaro, A. Needleman, Acta Metall. 31 (1983) 1951–1976.
[25] K.K. Mathur, P.R. Dawson, Int. J. Plast. 5 (1989) 67–94.
[26] R.J. Asaro, A. Needleman, Acta Metall. 6 (1985) 923–953.
[27] D. Pierce, R.J. Asaro, A. Needleman, Acta Metall. 30 (1982) 1087–1119.
[28] R.J. Asaro, Adv. Appl. Mech. 23 (1983) 1–115.
[29] D. Siebörger, H. Knake, U. Glatzel, Mater. Sci. Eng. A 298 (1-2) (2001) 26–33.
[30] H. Gao, Y. Huang, Scripta Mater. 48 (2) (2003) 113–118.
[31] D. Raabe, R. Becker, Model. Simul. Mater. Sci. Eng. 8 (2000) 445–462.
[32] D. Raabe, Annu. Rev. Mater. Res. 32 (2002) 53–76.
[33] A. Porter, B. Ralph, J. Mater. Sci. 16 (1981) 707–713.
[34] F.J. Humphreys, M. Hatherly, Recrystallization and Related Annealing Phenomena, 2nd ed., Elsevier, Amsterdam, 2004.
[35] A. Porter, B. Ralph, Mater. Sci. Eng. 59 (1983) 69–78.
[36] G. Gottstein, Acta Metall. 32 (7) (1984) 1117–1138.
[37] P. Haasen, Metall. Trans. A 24 (1993) 1001–1015.
[38] V. Randle, J. Mater. Sci. 40 (2005) 853–859.